Large-Scale InSAR Deformation Monitoring Using Realistic Simulation-Based Training of a Temporal Convolutional Network: Application to the Phlegraean Fields, Italy

Kourosh Shahryarinia[1,*], Mohammad Omidalizarandi[1], Ingo Neumann[1]

[1]Geodetic Institute, Leibniz University Hannover, Hannover, Germany
{kourosh.shahryari, zarandi, neumann}@gih.uni-hannover.de

Keywords: InSAR Time Series, Temporal Convolutional Networks, Deep Learning, Simulation-Based Training, Change Point Detection, Deformation Monitoring

Abstract

Large-scale land surface deformation monitoring using Interferometric Synthetic Aperture Radar (InSAR) requires robust detection of changes in long-term deformation trends. However, accurate change point (CP) detection remains challenging due to complex time series characteristics, including seasonal and quasi-periodic components and noise. Classical methods and many existing deep learning approaches rely on restrictive assumptions and training data that do not fully represent real-world InSAR time series, limiting their generalization and scalability in large-scale, real-world applications. In this study, we propose an integrated, fully supervised framework for CP detection in InSAR displacement time series based on Temporal Convolutional Networks (TCNs). The proposed TCN model employs dilated convolutions with multi-scale receptive fields to capture long-term temporal dependencies and complex deformation patterns, enabling robust identification of significant trend changes under noisy conditions. To effectively train this model, we introduce a deep learning-based InSAR time series simulation framework trained on real time series. This simulation framework produces physically consistent InSAR time series that retain essential temporal characteristics while introducing predefined, credible trend changes. Finally, we integrate the trained model into a large-scale anomalous change-detection pipeline that aggregates detected CPs from individual time series into spatially coherent deformation heatmaps suitable for operational monitoring. The proposed framework is evaluated using simulated data and real InSAR time series from the Phlegraean Fields caldera (Campi Flegrei), Italy. The results show clusters of anomalous behavior in the central Campi Flegrei–Pozzuoli area and in parts of Ischia and Procida, consistent with known unrest zones, associated periods, and independent measurements.

1. Introduction

Land surface deformation represents a significant hazard to urban areas and critical infrastructure networks, potentially leading to structural deterioration, economic losses, and increased risks to human safety. Continuous and reliable monitoring of deformation processes is therefore essential for early warning, risk assessment, and timely intervention. Interferometric Synthetic Aperture Radar (InSAR) has become a key technology for ground deformation monitoring because it provides spatially dense, nearly weather-independent, long-term, and millimetre-accurate displacement time series over wide areas by analysing the phase evolution of coherent radar targets (Ferretti et al., 2002). These time series provide an important basis for ground deformation monitoring across different applications, including the enhancement of geodetic reference systems and robust spatio-temporal modelling and quality assessment (Brockmeyer et al., 2020; Omidalizarandi et al., 2023). Changes in long-term deformation trends in InSAR displacement time series may indicate the development of instabilities in areas susceptible to deformation. The detection of these changes is commonly referred to as change point (CP) detection. Accurate CP detection remains challenging because real geophysical time series often contain complex trends, seasonal or quasi-periodic signals, correlated noise, atmospheric disturbances, and missing data (Osmanoğlu et al., 2016; Crosetto et al., 2016).

Classical methods for analysing trend changes in InSAR data mostly use linear or other parametric regression models together with statistical post-processing. Early multi-temporal InSAR approaches used frequent SAR acquisitions to better detect deformation changes and to describe displacement behaviour using predefined deformation models or deviation indices (Cigna et al., 2011, 2012). Subsequent statistical and user-oriented classification methods applied hypothesis tests and trend descriptors to group deformation histories into categories such as linear, quadratic, bilinear, or discontinuous, enabling semi-automatic analysis of large areas (Berti et al., 2013; Notti et al., 2015). Probabilistic and multiple-hypothesis-testing frameworks further improved the estimation of kinematic parameters and model selection in InSAR time series (Chang and Hanssen, 2015), while statistical change-detection schemes based on Sentinel-1 data were developed for continuous monitoring of ground deformation and for detecting offsets and gradient changes in displacement records (Raspini et al., 2018; Hussain et al., 2021). Other studies proposed recursive InSAR processing that combines amplitude and phase information with sequential hypothesis tests and Kalman filtering to detect deformation anomalies in near-real time (Hu et al., 2021), as well as Sequential Turning Point Detection (STPD) methods that estimate the timing and direction of trend changes in PS-InSAR displacement time series and relate them to hydrological or climatic drivers (Ghaderpour et al., 2024a,b,c). Although these developments substantially enhance the extraction of deformation information from InSAR data, important methodological constraints remain. Many frameworks still rely on relatively rigid parametric trend models and manually tuned decision thresholds, which can limit their adaptability under irregular sampling, missing data, or complex temporal patterns and reduce their effectiveness for describing multiscale deformation and detecting multiple low-magnitude changes along long InSAR displacement time series.

This contribution has been peer-reviewed. The double-blind peer-review was conducted on the basis of the full paper.
https://doi.org/10.5194/isprs-annals-XI-3-2026-269-2026

Recent studies have therefore explored deep learning approaches tailored to CP detection in InSAR time series. Lattari et al. (2022) proposed a supervised deep learning approach for CP detection in InSAR time series, combining Long Short-Term Memory (LSTM) and Time-Gated LSTM (TGLSTM) cells. The model is trained on simulated InSAR time series with known CPs, where LSTM units capture temporal dependencies and TGLSTM cells incorporate acquisition timing information. Their experiments demonstrate that the learned model is a valid alternative to a statistical reference method for CP detection and is effective when applied in real monitoring scenarios. Shahryarinia et al. (2025) further formulated CP detection as a supervised classification task using Bidirectional LSTM and U-Net–based architectures, supported by a dedicated simulation framework generating simulated InSAR time series with CPs under noisy conditions. Their models outperformed a Bayesian-based method in terms of standard detection metrics on both simulated and real InSAR time series, indicating improved accuracy and robustness for CP detection. Arya Fakhri and Satari (2025) introduced the Moving Average Large-Kernel Convolutional Neural Network (MALkCNN), which combines moving-average preprocessing with very large one-dimensional convolutional kernels to preserve long-term trends while suppressing short-term fluctuations. The model achieved higher accuracy and F1-scores than the TGLSTM baseline, with reduced computational complexity. Collectively, these studies demonstrate that recurrent and convolutional neural networks, when trained on simulated data and tailored to InSAR characteristics, can significantly improve CP detection compared to classical statistical approaches.

Despite recent progress, supervised deep learning approaches for CP detection still exhibit important limitations for large-scale, real-world deformation monitoring. Their performance is strongly dependent on the quality and realism of the training data; however, reliable ground-truth labels are generally unavailable in real InSAR time series because of noise, measurement uncertainty, and the complexity of deformation processes. As a result, most existing methods rely on synthetic data, whose simplified assumptions regarding deformation dynamics, seasonal or quasi-periodic behavior, and noise characteristics may reduce generalization under operational conditions. Furthermore, many current models are designed for specific input configurations or do not fully exploit the long-term temporal structure of the time series, which can limit their sensitivity to subtle, progressive, or nonstationary changes. In addition, only a limited number of studies have addressed the integration of such models into scalable processing frameworks capable of analyzing millions of InSAR time series and producing spatially coherent anomaly maps suitable for hazard monitoring and decision support

The main contributions of this work are summarized as follows:

1. A deep learning–based InSAR time series simulation framework is developed that generates realistic deformation time series with predefined CPs and includes seasonal, periodic, and noise components consistent with real InSAR time series.

2. A supervised Temporal Convolutional Network (TCN) architecture is specifically designed to detect long-term trend changes in InSAR time series, using multi-scale temporal convolutions and trained on realistic simulated time series to learn the CPs in the presence of noise in the data.

3. A large-scale anomalous CP detection pipeline is proposed, integrating the TCN model into an operational workflow and enabling the spatially coherent mapping of significant trend changes across extensive InSAR time series.

4. A comprehensive evaluation is conducted on real InSAR time series from the Phlegraean Fields (Italian: Campi Flegrei), Italy, including validation against independent GNSS measurements and comparison with previous studies, confirming the effectiveness and practicality of the proposed framework for large-scale deformation monitoring.

The subsequent sections are organized as follows: Section 2 describes the TCN-based CP detection model and the large-scale anomalous change detection approach. Section 3 describes the data and simulation framework. Section 4 presents and discusses the results obtained for both the simulated datasets and the real InSAR time series over the Phlegraean Fields, Italy. Finally, Section 5 summarizes the main findings and discusses the effectiveness of the proposed framework in real-world deformation monitoring scenarios.

2. Methodology

This section provides a concise overview of the proposed supervised architecture and its integration into a unified large-scale anomalous change detection framework. The objective of the study is to develop a supervised deep learning model capable of detecting long-term trend changes (CPs) directly from InSAR time series, even in the presence of noise and seasonal components.

In real-world InSAR time series, obtaining reliable ground-truth labels for supervised training is highly challenging due to gradual changes, ambiguous boundaries, and noisy radar measurements. To address this limitation, we employ a simulation-based training strategy to generate realistic InSAR time series with well-defined CPs as target labels. This approach allows the model to learn from a large number of physically consistent deformation scenarios with precise labels, thereby ensuring stable supervised optimization and improving its ability to distinguish true deformation patterns from noise-induced fluctuations and to generalize effectively to real InSAR time series.

Overall, the methodology is structured as follows: First, the architecture of the supervised TCN-based model is presented in Subsection 2.1. Next, the integration of these components into a unified large-scale anomalous change detection framework is described in Subsection 2.2, together with the overall workflow illustrated in Figure 2. Finally, the procedure for generating realistic simulated InSAR time series for training is presented in Subsection 3.1.

2.1 Temporal Convolutional Network (TCN)

We developed a supervised deep learning model based on TCN combined with standard convolutional layers for long-term anomalous change detection in InSAR time series. The network predicts per-epoch anomaly probabilities at full temporal resolution, enabling the identification of subtle and persistent deformation behaviors across time.

Before training, all input time series were normalized and detrended to improve numerical stability and remove large-scale linear trends unrelated to deformation time series. Each time series was normalized independently using its own mean and

standard deviation. Each time series was normalized independently using its own mean and standard deviation. The normalization was performed as follows:

$$\tilde{\mathbf{x}} = \frac{\mathbf{x} - \mu}{\sigma}, \tag{1}$$

where $\mu = \mathrm{mean}(\mathbf{x})$ and $\sigma = \mathrm{std}(\mathbf{x})$.

The first stage of the network consists of multiple Multi-Dilation TCN blocks, each containing several one-dimensional convolutional layers with distinct dilation rates. This structure allows the receptive field to expand exponentially while maintaining the original sequence length. For an input sequence $\mathbf{x} \in \mathbb{R}^{C \times L}$, the dilated convolution with dilation factor d and kernel size K is defined as

$$\mathbf{y}(t) = \sum_{k=0}^{K-1} w_k, \mathbf{x}(t - d \cdot k), \tag{2}$$

where t denotes the time index, w_k are learnable convolutional weights, and d determines the spacing between the sampled input positions. Thus, the output at time t depends on a wider temporal context than in standard convolution, allowing efficient modeling of long-range temporal dependencies without recurrent connections (Bai et al., 2018).

Following the TCN encoder, a lightweight local Convolutional Neural Network (CNN) module refines the extracted features through consecutive convolutional and nonlinear activation layers, enhancing local smoothness and temporal consistency in the predicted deformation patterns. Average pooling aggregates temporal features into a compact representation, which is then projected back to the original sequence length through a fully connected head. A sigmoid activation function produces per-epoch anomaly probabilities $\hat{y}_t \in [0, 1]$. The model was optimized using a mean squared error (MSE) loss function, which ensured smooth gradient propagation and stable learning, particularly under gradual or ambiguous anomaly transitions. For the predicted anomaly probabilities $\hat{y}_t$ and the corresponding reference labels y_t, the loss function was defined as:

$$\mathcal{L}_{\mathrm{PD}} = \frac{1}{L} \sum_{t=1}^{L} (\hat{y}_t - y_t)^2, \tag{3}$$

This objective encourages smooth and continuous predictions, promoting stable optimization even in the presence of noisy time series during training.

The model was trained for 200 epochs with early stopping using the Adam optimizer (Kingma and Ba, 2014), with a learning rate of 1×10^{-3} and weight decay of 1×10^{-4}. Training was performed using mini-batches of size 64. Detected probabilities were converted into anomaly labels using $\tau = 0.5$, as this value is commonly used as the standard decision threshold in classification. This configuration enabled robust convergence and stable performance for detecting long-term, low-magnitude deformation anomalies in InSAR time series.

Figure 1 illustrates the proposed TCN-based supervised architecture, which integrates multi-scale temporal encoding with local spatial refinement to achieve sensitive and robust detection of long-term anomalous deformation changes in noisy and seasonally affected InSAR time series.

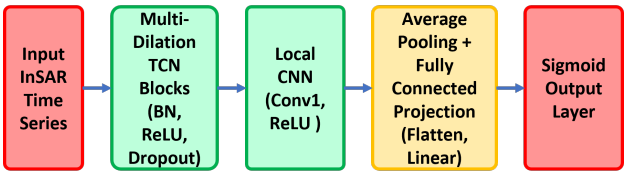

Figure 1. Architecture of the proposed TCN-based supervised model for long-term anomalous change detection in InSAR time series.

2.2 Large-Scale Anomalous Change Detection Approach

To analyze anomalies at large and regional scales, we followed a stepwise strategy, as shown in Figure 2. To train the TCN model using realistic time series, a simulation process was developed, which is discussed in Subsection 3.1. After training both networks on simulated data, the best-performing models with their saved weights were applied to real InSAR time series for change detection. For each time series, a detected change in the long-term trend was accepted when its probability exceeded 0.5, indicating that a change was more likely than no change.

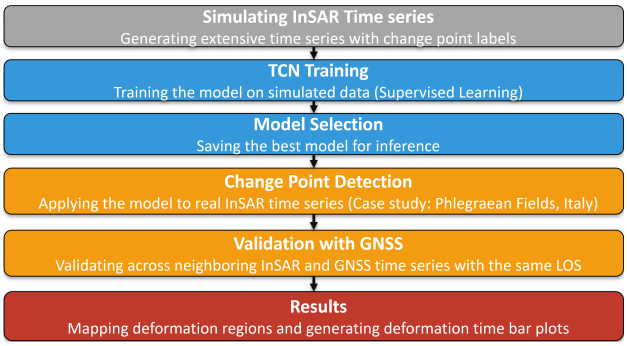

Figure 2. Flowchart of the proposed large-scale anomalous deformation monitoring framework.

To evaluate the model’s performance on real data, an extensive set of real InSAR time series was used. The detected deformation trends were further validated by comparison with displacement time series obtained from nearby GNSS stations projected into the line-of-sight (LOS) direction within the same area (Giudicepietro et al., 2024b). Finally, the significant anomalies were discussed, and two spatial anomaly maps were constructed, in which anomalous deformation regions are indicated by warmer colors.

3. Data Specification

3.1 Simulation of InSAR Time Series

We simulated InSAR time series through a multi-step pipeline based on a subset of real InSAR time series. The long-term trend was removed using a cubic smoothing spline based on a B-spline basis, implemented using the UnivariateSpline function in SciPy (Virtanen et al., 2020). The smoothing parameter was selected based on Silverman’s rule of thumb (Silverman, 1985) to maintain a balance between accurately fitting the data and achieving a smooth trend. Values exceeding $\pm 2\sigma$ were excluded from the spline fitting process to mitigate the influence of outliers. After detrending, residuals corresponding to outlier timestamps in the raw series were clipped to the $\pm 2\sigma$ range and re-centered to zero mean to remove amplitude shifts. To ensure

temporal consistency and suitability for modeling, we applied the Augmented Dickey–Fuller (ADF) test (Dickey and Fuller, 1979) to verify stationarity and excluded non-stationary time series from further analysis.

Next, we trained a Temporal Convolutional Variational Autoencoder (TCN-VAE) to learn the underlying distribution of the detrended time series and to generate new, realistic time series from its latent space. The model integrates TCN with variational inference to obtain a compact latent representation of InSAR time series while preserving their temporal dependencies. The encoder consists of three residual TCN blocks with a kernel size of 3, a dropout rate of 0.2 (Srivastava et al., 2014), and dilation factors of $\{1, 2, 4\}$, followed by average pooling for temporal downsampling. It maps the input sequence into latent mean and variance vectors, from which a latent variable is sampled using the reparameterization trick. The decoder mirrors the encoder with three transposed convolutional blocks that expand the latent features to 256 channels and reconstruct time series of length 300. The latent space dimension was set to 128. Model training was performed for 100 epochs with a batch size of 64 using the Adam optimizer (Kingma and Ba, 2014) (learning rate 1×10^{-3}, weight decay 1×10^{-4}) and early stopping. The loss function combined a reconstruction term with the Kullback–Leibler (KL) divergence (Kingma and Welling, 2013), weighted by a factor β, to promote smooth and regularized latent representations.

Figure 3 shows three randomly selected detrended InSAR time series obtained from this procedure. The blue dotted lines correspond to real detrended time series used as training inputs for the TCN-VAE model, while the red dotted lines represent simulated time series generated from the model’s latent space. Displaying them together provides a clear visual comparison and illustrates the strong similarity between the real and generated time series.

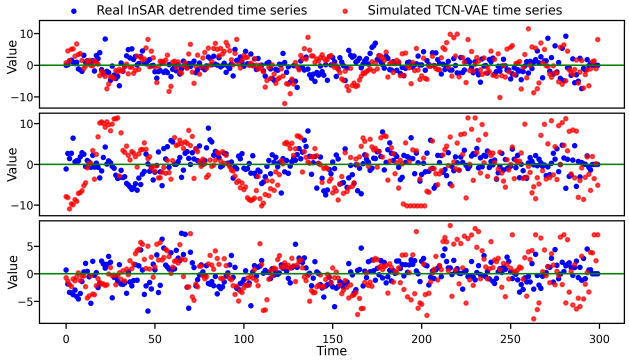

Figure 3. Comparison between real detrended InSAR time series (blue) and simulated series generated from the learned latent distribution (red).

To further validate this similarity, we extract the five dominant frequency components from each time series and compare their distributions using a histogram, as shown in Figure 4. Frequencies are expressed in cycles per year, reflecting the temporal sampling interval of the dataset. Both real and generated time series exhibit most of their spectral energy between 0 and 3 cycles per year, with only a few higher-frequency contributions. The strong overlap between the two distributions indicates that the TCN-VAE effectively preserves the key spectral characteristics of real InSAR time series.

Finally, we imposed a piecewise-linear trend with up to three randomly placed CPs on each generated time series, yielding simulated InSAR time series with known deformation changes.

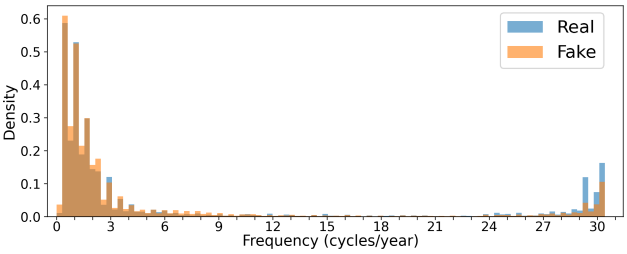

Figure 4. Histogram of the frequencies from real and generated detrended InSAR time series, showing strong spectral similarity.

To enhance realism and variability, we employed an adaptive trend-change generator that introduces slope variations at random locations while enforcing constraints on both spacing and magnitude, inspired by Arya Fakhri and Satari (2025). The generator produces smooth Gaussian-like CP labels (Lattari et al., 2022), where, for each CP c_i, a soft target is defined as

$$g_i(t) = \exp\left(-\frac{1}{2}\left(\frac{t - c_i}{\sigma_i}\right)^2\right), \tag{4}$$

with σ_i controlling the spread (uncertainty) around the CP. The standard deviation σ_i is adaptively determined based on the local noise level $\sigma_{\text{noise},i}$ and the slope change magnitude Δs_i as

$$\sigma_i = \alpha \cdot \frac{\sigma_{\text{noise},i}}{|\Delta s_i| + \varepsilon}, \tag{5}$$

where α is a scaling factor and ε is a small constant for numerical stability. This formulation yields narrower Gaussians for strong, well-defined slope changes and broader Gaussians for weaker or noisier transitions. In total, we generated 10,000 simulated time series, including cases with and without CPs, allowing the models to learn both deformation and no-change scenarios.

3.2 EGMS Real InSAR Time series Data

The European Ground Motion Service (EGMS) Calibrated 2019–2023 product (European Environment Agency, 2024) contains ground displacement time series generated from Copernicus Sentinel-1 InSAR observations across Europe. Each measurement point corresponds to a line-of-sight (LOS) displacement time series acquired at 6–12-day intervals. The dataset includes both ascending and descending satellite tracks, offering complementary perspectives on surface deformation. These time series capture subtle ground motions, such as subsidence, uplift, and landslides, making them highly suitable for large-scale deformation monitoring and change analysis. Section 4.1.1 presents the Campi Flegrei case study and the corresponding InSAR time series, together with the GPS data used for validation, in a combined figure.

4. Results and Discussion

4.1 Model Performance on Simulated Time Series

As described in Section 2, the models were evaluated on simulated InSAR time series using an 80% training and 20% validation split. As shown in Table 1, the TCN model achieved strong performance, with an F1 of 0.891 and an F2 of 0.889. The F1 was used for model selection, while the F2 further supports the

model’s ability to detect true positives. Uncertainty in the target CPs was taken into account by counting predictions within the uncertain target region as true positives, and predictions were obtained by retaining peaks in the output probability distribution with values ≥ 0.5. Overall, the results indicate that the TCN model performs effectively for CP detection in simulated InSAR time series.

Table 1. Performance metrics of the TCN model on validation set of simulated data.

F1	F2	Precision	Recall
0.891	0.889	0.893	0.888

Figure 5 illustrates the performance of the TCN model on three randomly selected simulated time series from the validation set that were not used during training. In the first subplot, the three simulated time series (previously marked with red dots in Figure 3) are shown after applying our piecewise-linear trends; the second subplot presents their corresponding target labels in matching colors. It is evident that the light blue time series (TS 3) does not exhibit any trend changes, and such stable series are deliberately included in the training data so that the model also learns to recognize stationary time series, which are later used during the validation phase after saving the best-performing model. The third subplot displays the predicted CP probabilities of the TCN model, which successfully identified the true CPs and correctly assigned no significant probability to TS 3. Despite some noise in the predicted probabilities, the primary peaks closely correspond to the true CPs, demonstrating that the simulated data effectively retain the noise characteristics of real EGMS time series and that the proposed model maintains strong detection robustness in the presence of irregular and periodic variations.

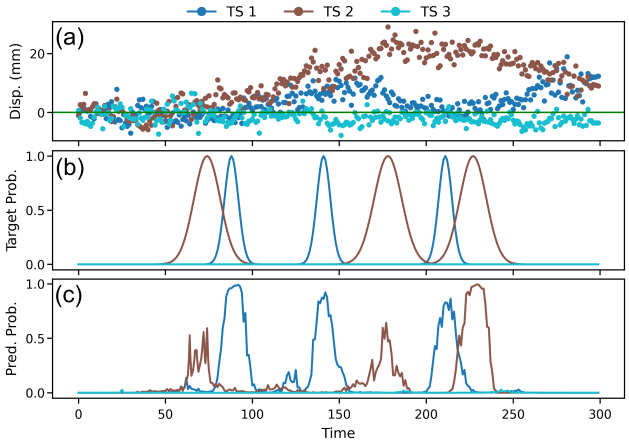

Figure 5. TCN model results on randomly selected simulated time series: (a) simulated time series, (b) Gaussian CP targets, and (c) detected CP probabilities. Each time series includes its corresponding target and detection results, shown in the same color.

The strong performance of the proposed TCN model can be attributed to its ability to learn the temporal dynamics of InSAR displacement time series. By employing multi-scale dilated convolutional layers, the model effectively captures both short-term variations and long-term deformation trends, which are essential for detecting CPs. This architecture enables the network to distinguish random short-term fluctuations from continuous and physically meaningful deformation events. Moreover, the convolutional design inherently suppresses high-frequency noise, making the model robust to atmospheric effects and seasonal patterns commonly observed in InSAR data. Overall, these characteristics make the TCN architecture highly suitable for detecting gradual and subtle deformation changes in noisy and complex time series.

4.1.1 Model Performance on EGMS Data – Phlegraean Fields, Italy

After training the model on a large set of simulated InSAR time series (Section 3.1), including both deforming and stable time series, the best-performing weights were selected using early stopping. We then applied the trained model to real EGMS InSAR time series from the Phlegraean Fields in Italy. The overall workflow is summarized in Figure 2.

The Phlegraean Fields is a densely urbanized volcanic caldera near Naples and is considered one of the highest-risk volcanic areas in Europe. Over the last two decades, it has shown persistent unrest, with long-term uplift, increased seismicity, and enhanced geochemical activity. The deformation field is typically characterized by an axisymmetric, bell-shaped uplift centered in the caldera, with cumulative uplift of about 1.2 m at the center since 2005 (Giudicepietro et al., 2024a). This makes the area an ideal test site for continuous InSAR and GNSS monitoring. Figure 6 shows the study area and the distribution of GNSS stations.

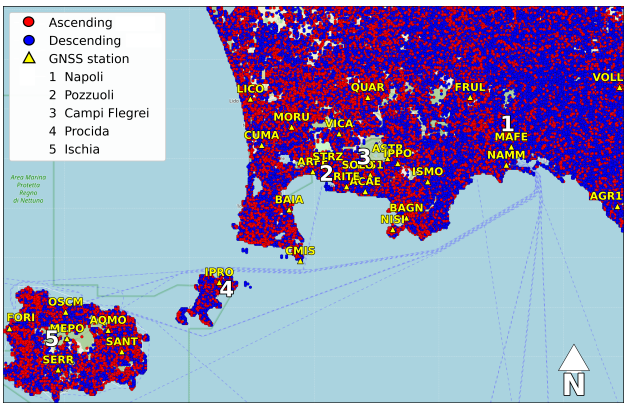

Figure 6. Phlegraean Fields, Italy. ascending and descending time series and the distribution of GNSS stations are shown.

In order to validate and compare the detected CPs between GNSS and EGMS InSAR time series, we implemented a consistent three-step workflow: (i) spatial pairing of GNSS stations and InSAR time series, (ii) projection of GNSS displacements onto the InSAR LOS, and (iii) temporal alignment and coherence assessment.

(i) Spatial pairing of GNSS and InSAR time series: For each GNSS station with known coordinates (ϕ_s, λ_s), we searched for the nearest InSAR point by minimizing the great-circle distance using the haversine formula (Sinnott, 1984):

$$d = 2R \arcsin\left(\sqrt{\sin^2\left(\frac{\Delta\phi}{2}\right) + \cos(\phi_s)\cos(\phi_i)\sin^2\left(\frac{\Delta\lambda}{2}\right)}\right), \tag{6}$$

where $R = 6{,}371{,}000$ m is the mean Earth radius, and (ϕ_i, λ_i) are the geographical coordinates of each candidate InSAR point.

(ii) Projection of GNSS onto the InSAR LOS: For the selected InSAR point, we used the LOS unit vector components (l_E, l_N, l_U) provided in the EGMS products, which represent the sensitivity of the satellite measurements to displacement in the east, north, and up directions, respectively. The

three-dimensional GNSS displacements $(E(t), N(t), U(t))$, expressed in meters, were projected onto the InSAR LOS to obtain a one-dimensional LOS displacement following the standard LOS projection formulation (Hanssen, 2001; Tondaś et al., 2023; Delen and Balik Sanli, 2024):

$$\mathrm{GNSS}_{\mathrm{LOS}}(t) = E(t)\, l_E + N(t)\, l_N + U(t)\, l_U. \tag{7}$$

This step ensures that GNSS and InSAR describe motion along the same viewing direction, which is essential because InSAR does not directly measure the east, north, and up displacement components separately. By expressing both datasets in the LOS frame, we can directly compare their deformation magnitudes and temporal patterns.

(iii) Temporal alignment and coherence assessment: To enable point-by-point comparison, we aligned the GNSS time series projected onto the LOS with the InSAR acquisition dates of the corresponding InSAR time series. The GNSS values were linearly interpolated to these acquisition dates to obtain paired measurements (Delen and Balik Sanli, 2024; Crosetto et al., 2016), while leaving the original InSAR time series unchanged. The analysis was restricted to the observation period covered by the EGMS time series so that both datasets represented the same deformation interval.

For each GNSS–InSAR pair, we quantified the temporal coherence between GNSS and InSAR using the Pearson correlation coefficient (Rodgers and Nicewander, 1988; Benesty et al., 2009):

$$r = \frac{\sum_k \left(\mathrm{GNSS}_{\mathrm{LOS}}(t_k) - \overline{\mathrm{GNSS}}_{\mathrm{LOS}}\right)\left(\mathrm{InSAR}_{\mathrm{LOS}}(t_k) - \overline{\mathrm{InSAR}}_{\mathrm{LOS}}\right)}{\sqrt{\sum_k \left(\mathrm{GNSS}_{\mathrm{LOS}}(t_k) - \overline{\mathrm{GNSS}}_{\mathrm{LOS}}\right)^2 \sum_k \left(\mathrm{InSAR}_{\mathrm{LOS}}(t_k) - \overline{\mathrm{InSAR}}_{\mathrm{LOS}}\right)^2}} \tag{8}$$

In the above equation, r denotes the Pearson correlation coefficient, $k = 1, \ldots, K$ indexes the paired acquisition dates, $\mathrm{GNSS}_{\mathrm{LOS}}(t_k)$ and $\mathrm{InSAR}_{\mathrm{LOS}}(t_k)$ are the paired GNSS and InSAR LOS displacement values at date t_k, and the overbars denote sample means. The numerator is proportional to the sample covariance, and the denominator is the product of the sample standard deviations. Pearson’s r is used here as a simple, dimensionless measure of temporal agreement. Because it is insensitive to constant offsets and linear scaling, it reflects how well the two time series follow the same temporal deformation pattern.

Figure 7 illustrates the joint analysis for three representative stations (MORU, ACAE, and LICO), showing the $\mathrm{GNSS}_{\mathrm{LOS}}$ time series and their corresponding $\mathrm{InSAR}_{\mathrm{LOS}}$ time series. For each site, we use the paired time series defined in Section 4.1.1: (i) the InSAR LOS time series of the closest InSAR point and (ii) the GNSS time series projected into the same LOS and sampled at the corresponding EGMS acquisition dates. As an independent reference for CP interpretation, BEAST (Zhao et al., 2019), a Bayesian ensemble approach for time series decomposition and CP detection, was applied exclusively to the $\mathrm{GNSS}_{\mathrm{LOS}}$ time series. In the upper subplot, solid lines represent the $\mathrm{GNSS}_{\mathrm{LOS}}$ displacements, while dashed lines show the corresponding $\mathrm{InSAR}_{\mathrm{LOS}}$ displacements of the nearest InSAR time series. Both series are plotted in the same LOS reference frame and on matching acquisition dates, allowing a direct visual comparison of their temporal evolution. The lower subplot shows the CP probabilities over time, obtained by applying BEAST to the $\mathrm{GNSS}_{\mathrm{LOS}}$ data. The InSAR series are included for visual reference only, demonstrating that both datasets exhibit consistent deformation trends and that the GNSS time series are correctly projected into the InSAR LOS direction.

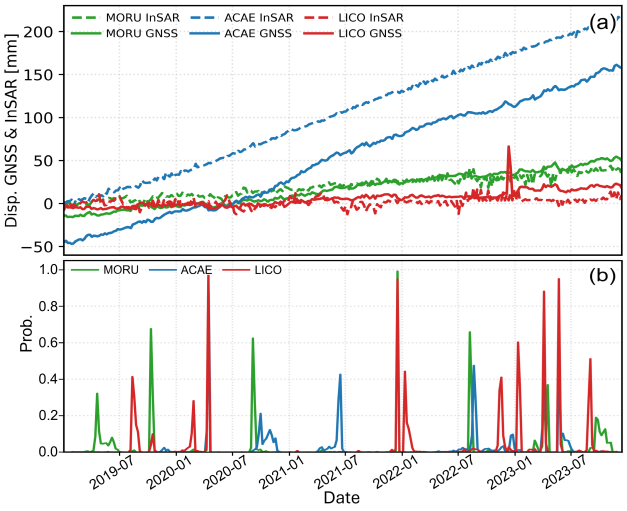

Figure 7. Comparison of LOS displacement time series and BEAST-derived CP probabilities for three representative stations (MORU, ACAE, and LICO). (a) $\mathrm{GNSS}_{\mathrm{LOS}}$ (solid) and nearby LOS InSAR time series (dashed) time series, both projected into the same LOS geometry and sampled on common acquisition dates. (b) BEAST CP probabilities obtained exclusively from the $\mathrm{GNSS}_{\mathrm{LOS}}$ time series. The InSAR data are shown only for visual comparison, highlighting their consistency with the GNSS deformation trends.

These examples show that the projected $\mathrm{GNSS}_{\mathrm{LOS}}$ and the nearest InSAR time series exhibit very similar deformation trends at all three stations. The similarity in slope and relative amplitude indicates that the LOS projection, temporal alignment, and GNSS–InSAR pairing are consistent. Moreover, the main peaks in the BEAST CP probabilities correspond to visible changes in the LOS displacement measurements, supporting the reliability of the detected CPs and the overall integration of the GNSS and InSAR time series.

As introduced above, we applied our best-performing model to the LOS InSAR time series to enable a large-scale analysis of ground deformation. In total, approximately 4,850,000 InSAR time series were processed across the study area (Ascending: 1,936,289; Descending: 2,913,711). To illustrate the local performance of the LOS projection and the model predictions, we focus on the MORU station ($\phi = 40.859°$, $\lambda = 14.082°$) and its nearby InSAR time series in the ascending geometry.

Figure 8 shows that the InSAR time series closely match the uplift trend observed in the projected $\mathrm{MORU}_{\mathrm{LOS}}$ GNSS data. This confirms that the LOS projection and the matching between GNSS and InSAR measurements are reliable. In the lower subplot, the main peaks in the CP probabilities from the InSAR data occur close to those detected by BEAST in the $\mathrm{MORU}_{\mathrm{LOS}}$ GNSS series. Some of these peaks also match visible changes in the slope of the displacement curves. Some differences between the BEAST and TCN results are expected. BEAST analyzes a single, low-noise GNSS time series and can detect small slope variations. In contrast, the TCN model works on noisier InSAR time series and is trained to focus on strong, long-term deformation patterns while ignoring short-term fluctuations caused by atmospheric effects or decorrelation noise. As a result, BEAST may detect some small changes that appear with lower probability in the TCN output, reflecting the different noise levels in

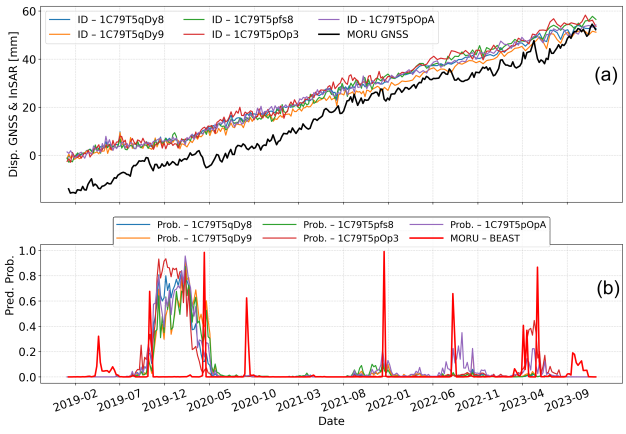

Figure 8. InSAR ascending track. (a) projected MORU_{LOS} GNSS displacement (black) and LOS InSAR time series of nearby InSAR time series (colors), all expressed in the same LOS reference frame for direct comparison. (b) CP probabilities detected by the TCN model for the InSAR time series and BEAST CP probabilities derived from MORU_{LOS}.

the two datasets and the more cautious, large-scale detection behavior of the TCN model.

Since individual InSAR time series may exhibit different noise levels and local irrigularities, some high CP probabilities may reflect only local effects. To highlight regionally relevant changes over the Phlegraean Fields, we retain only InSAR time series results with detected CP probability ≥ 0.5 and, for each month m, compute the percentage of anomalous InSAR time series as

$$f_m = 100 \cdot \frac{A_m}{N_m}, \tag{9}$$

where N_m is the total number of InSAR time series in month m and A_m is the number with probability ≥ 0.5. This metric reflects the share of anomalous InSAR time series rather than raw counts. Figure 9 show f_m for the ascending and descending geometries, respectively. Most months exhibit very low values, while a few distinct peaks indicate periods when many InSAR time series simultaneously show significant changes, helping to distinguish spatially coherent deformation episodes from isolated detections caused by noise or data gaps. Although more time series are available in the descending geometry, the anomaly fractions f_m show that a larger share of ascending time series is classified as anomalous, suggesting that the ascending track is more sensitive to the dominant deformation time series and/or less affected by decorrelation in key periods. The most significant changes are those months where both ascending and descending geometries display elevated f_m simultaneously, indicating deformation time series that are consistent across acquisition geometries rather than driven by track-specific noise or purely local effects. This joint increase in anomaly fractions confirms that these episodes affect a substantial portion of the study area.

To visualize where CPs occur most frequently across the study area, we generated geolocated heatmaps separately for the ascending and descending datasets, as shown in Figure 10. For each InSAR time series, we counted the number of acquisition times during which the detected CP probability exceeded 0.5. These counts were then spatially aggregated using hexagonal bins, and the resulting values, referred to as the Peak Intensity, were used as the color scale for the maps. High intensities indic-

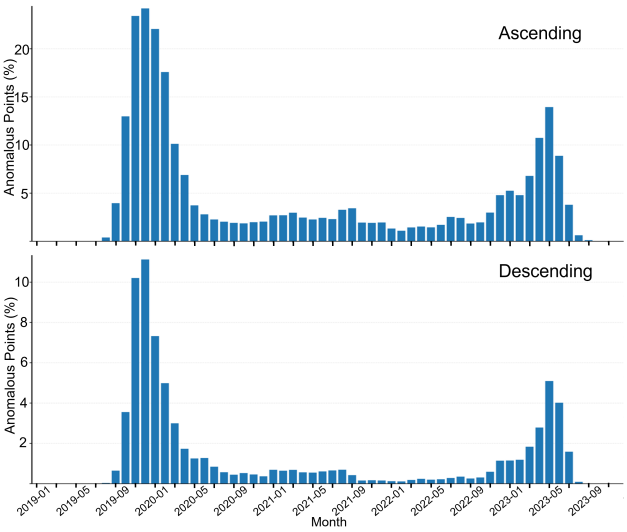

Figure 9. Monthly fraction (%) of InSAR time series classified as anomalous (detected CP probability ≥ 0.5) for ascending and descending geometries.

ate regions where many InSAR time series repeatedly exhibit high-probability CPs, whereas low values correspond to sparse or isolated detections.

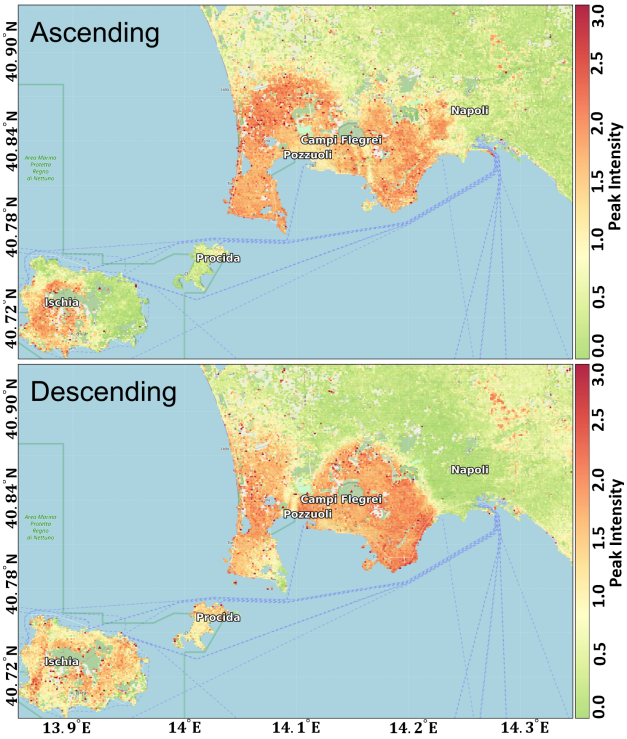

Figure 10. Spatial distribution of CP peak intensity (Number of peaks with probability bigger than 0.5) for ascending and descending geometries.

4.1.2 Consistency check of our results with previous studies

(a) Temporal consistency with other studies: Figure 9 show the monthly fraction of anomalous InSAR time series for the ascending and descending datasets. Both geometries highlight two dominant clusters: an increase between October 2019 and May 2020 and a more pronounced rise from late 2022 to mid 2023, with peak values in early 2023. The 2019–2020 cluster

This contribution has been peer-reviewed. The double-blind peer-review was conducted on the basis of the full paper.
https://doi.org/10.5194/isprs-annals-XI-3-2026-269-2026 | © Author(s) 2026. CC BY 4.0 License.

occurs during the high-rate inflation phase at Phlegraean Fields documented by continuous GPS and MT-InSAR analyses, which report sustained uplift and accelerating deformation up to the end of 2019 (De Martino et al., 2021; Bevilacqua et al., 2022; Polcari et al., 2022). The second cluster, from late 2022 to mid 2023, coincides with the most recent escalation of unrest, characterized by the highest uplift rates and a modified deformation pattern inferred from multi-sensor observations (Giudicepietro et al., 2024a; Astort et al., 2024). The consistency of these temporal patterns across both ascending and descending tracks indicates that the detected anomalies are linked to real deformation processes rather than noise or model instabilities.

To assess the geophysical plausibility of the detected anomalies in more detail, we compare our results with key geodetic studies of the Phlegraean Fields. De Martino et al. (2021) analyse twenty years of continuous GPS measurements (2000–2019) and show a long-lasting uplift, with a marked acceleration after 2005 and a cumulative vertical displacement of about 65 cm at Pozzuoli by the end of 2019. Our first anomaly cluster between late 2019 and mid 2020 occurs at the end of this high-rate inflation phase, consistent with an enhanced deformation state identified independently by GPS. Bevilacqua et al. (2022) jointly investigate GPS and seismicity from 2000 to 2020 and identify unsteadily accelerating uplift and rate maxima in the years preceding 2020; the increased fraction of anomalous time series in 2019–2020 agrees with these phases of enhanced uplift and seismic activation. Polcari et al. (2022) construct a homogeneous multi-mission MT-InSAR displacement dataset for 1992–2021 and confirm persistent inflation and elevated deformation rates during the late 2010s; our 2019–2020 anomalies fall within this interval and are therefore consistent with the long-term InSAR-derived uplift history. Matano et al. (2025) develop an MT-InSAR-based procedure (2016–2021) to isolate secondary vertical deformation anomalies superimposed on the main bowl-shaped uplift. Their identification of spatially coherent deviations from the average pattern is conceptually consistent with the clustered anomalous regions produced by our framework, indicating that our large-scale anomaly detection extends this anomaly-based view beyond 2021.

For the recent unrest, Giudicepietro et al. (2024a) use InSAR and GNSS data to characterise the 2021–2023 escalation and report a localized geodetic anomaly with an uplift deficit in the eastern sector of the caldera relative to the surrounding uplift pattern. Our second anomaly cluster, with a pronounced increase from late 2022 to mid 2023, overlaps this interval and is consistent with the onset and development of this geodetic anomaly. Astort et al. (2024) integrate geodetic and modelling results for 2007–2023 and show that the highest uplift rates occur in the most recent phases (2020–2023); the peak anomaly fractions we obtain in early 2023 coincide with these high-rate intervals, reinforcing the interpretation that our framework captures the strongest stage of the ongoing unrest. Taken together, the agreement in timing between our anomaly clusters and these independent geodetic results supports the conclusion that the detected anomalies primarily reflect real deformation processes at Phlegraean Fields.

(b) Spatial consistency of anomalous deformation patterns: The spatial distribution of anomalous time series (Figure 10) reveals coherent clusters concentrated within the Phlegraean Fields, with the highest densities located in the central sector during the 2019–2020 anomaly period and extending towards the eastern sector during the 2022–2023 anomaly period. During October 2019–May 2020, anomalous time series are mainly focused around the area of maximum uplift near Pozzuoli, in line with the deformation pattern reported by GPS and MT-InSAR studies (De Martino et al., 2021; Bevilacqua et al., 2022; Polcari et al., 2022). In late 2022–mid 2023, anomalous clusters intensify and partially shift towards the eastern caldera, consistent with the localized geodetic anomaly and modified uplift pattern described by Giudicepietro et al. (2024a) and with the high-rate unrest phase outlined by Astort et al. (2024).These spatially coherent patterns are also compatible with the secondary deformation anomalies identified in MT-InSAR-based analyses for 2016–2021(Matano et al., 2025). We also find that the spatial distribution of our geolocated heatmaps is consistent with the EGMS interactive online map. As shown in Figure 11, the largest velocity differences appear in the Campi Flegrei–Pozzuoli area, which is in agreement with our spatial maps. This indicates that the most significant CPs also occur in this region, which has been highly active due to seismic and volcanic processes in recent years. Figure 11 also shows a similar anomalous pattern, driven by the magnitude of the velocity change, in parts of Ischia and Procida, consistent with our heatmaps.

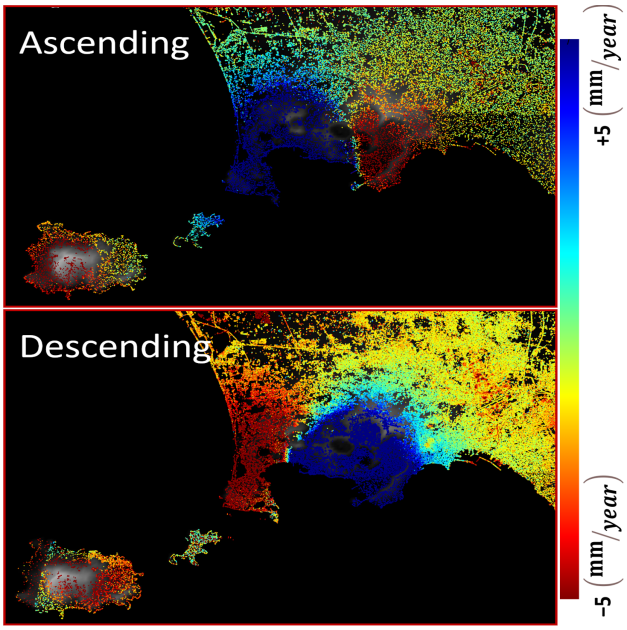

Figure 11. EGMS ascending and descending InSAR time series maps obtained from the EGMS website. The color bar indicates the mean velocity (mm/year).

The combined temporal and spatial consistency between our results and previous studies supports the reliability of the proposed simulation-trained TCN framework as a tool for large-scale deformation monitoring at Phlegraean Fields.

5. Conclusion

In this work, we developed a framework for detecting CPs in large-scale InSAR time series and applied it to the Phlegraean Fields caldera. The approach combines simulation-based training, a TCN-based model for estimating CP probabilities from LOS InSAR time series, and systematic consistency checks with independent GNSS measurements.

By projecting GNSS displacements onto the InSAR LOS and pairing each GNSS station with the nearest InSAR time series, we demonstrated that the resulting LOS displacement time series

show strong agreement for a set of randomly selected GNSS stations. The strong consistency between the projected GNSS and nearby InSAR time series, together with the comparison against CPs detected by the BEAST method, confirms that the GNSS–InSAR integration is robust and that the model successfully detects the significant deformation changes identified in the GNSS data. In some cases, BEAST identifies subtle changes as significant, but our model assigns lower probabilities to them, which mainly reflects the different objectives of the two methods. BEAST is used to detect small changes in clean, low-noise GNSS data, while the TCN model focuses on long-term deformation patterns in noisier InSAR data and handles fluctuations caused by the inherently noisy nature of InSAR measurements.

We applied the trained model to approximately 4.85 million EGMS InSAR time series in ascending and descending geometries and summarized detections using monthly anomaly fractions, i.e., the percentage of time series with high CP probability in each month. Although more time series are available in the descending geometry, a larger proportion of ascending InSAR time series are classified as anomalous during key periods, suggesting a higher sensitivity of the ascending track to the dominant LOS deformation signal. Geolocated maps of CP peak intensity provide a spatial overview of where high-probability CPs occur most frequently. Both geometries highlight coherent clusters in the central Campi Flegrei–Pozzuoli area and in parts of Ischia and Procida, consistent with known unrest zones and independent measurements. The similar spatial patterns in the ascending and descending data suggest that the detected CPs reflect real ground deformation, rather than geometry-related distortions or isolated noisy scatterers.

Overall, the proposed framework (1) simulates realistic InSAR time series derived from real InSAR time series with known labels, (2) scales to millions of InSAR time series, and (3) generates temporally and spatially explicit results that enable the identification of coherent deformation periods over large regions. These results demonstrate that the method is well suited as a supporting tool for continuous monitoring of the Phlegraean Fields and can be extended to other volcanic and urban areas.

Future work will focus on incorporating additional in situ data into the network and analyzing each GNSS station together with its surrounding InSAR time series to obtain more localized results. A limitation of this study is that each InSAR point is analyzed independently, without considering neighboring points. For large-scale applications, investigating spatiotemporal relationships among InSAR points may further improve the analysis.

Acknowledgements

This publication has been prepared using European Union’s Copernicus Land Monitoring Service information. The InSAR displacement time series used in this study were obtained from the European Ground Motion Service (EGMS) Calibrated 2019–2023 product: https://doi.org/10.2909/8889e0a7-a6df-47a8-b4e7-a9cb32cbbf6b.

Funding

This research was supported by the Deutscher Akademischer Austauschdienst (DAAD) through the funding programme *Research Grants – Doctoral Programmes in Germany, 2024/25* (Funding ID: 57693453).

References

Arya Fakhri, S., Satari, M., 2025. Trend change point detection in InSAR derived displacement time series using MALkCNN: A deep learning approach. *PFG–Journal of Photogrammetry, Remote Sensing and Geoinformation Science*, 1–16.

Astort, A., Trasatti, E., Caricchi, L., Polcari, M., De Martino, P., Acocella, V., Di Vito, M. A., 2024. Tracking the 2007–2023 magma-driven unrest at Campi Flegrei caldera (Italy). *Communications Earth & Environment*, 5(1), 506.

Bai, S., Kolter, J. Z., Koltun, V., 2018. An empirical evaluation of generic convolutional and recurrent networks for sequence modeling. *arXiv preprint arXiv:1803.01271*. https://arxiv.org/abs/1803.01271.

Benesty, J., Chen, J., Huang, Y., Cohen, I., 2009. Pearson correlation coefficient. *Noise reduction in speech processing*, Springer, 1–4.

Berti, M., Corsini, A., Franceschini, S., Iannacone, J. P., 2013. Automated classification of persistent scatterers interferometry time series. *Natural Hazards and Earth System Sciences*, 13(8), 1945–1958.

Bevilacqua, A., De Martino, P., Giudicepietro, F., Ricciolino, P., Patra, A., Pitman, E. B., Bursik, M., Voight, B., Flandoli, F., Macedonio, G. et al., 2022. Data analysis of the unsteadily accelerating GPS and seismic records at Campi Flegrei caldera from 2000 to 2020. *Scientific Reports*, 12(1), 19175.

Brockmeyer, M., Schnack, C., Jahn, C.-H., 2020. Datenanalyse und flächenhafte Modellierung der PSI-Informationen des Bodenbewegungsdienstes Deutschlands für die Landesfläche Niedersachsens. *zfv – Zeitschrift für Geodäsie, Geoinformation und Landmanagement*.

Chang, L., Hanssen, R. F., 2015. A probabilistic approach for InSAR time-series postprocessing. *IEEE Transactions on Geoscience and Remote Sensing*, 54(1), 421–430.

Cigna, F., Del Ventisette, C., Liguori, V., Casagli, N., 2011. Advanced radar-interpretation of InSAR time series for mapping and characterization of geological processes. *Natural Hazards and Earth System Sciences*, 11(3), 865–881.

Cigna, F., Tapete, D., Casagli, N., 2012. Semi-automated extraction of deviation indexes (DI) from satellite persistent scatterers time series: Tests on sedimentary volcanism and tectonically-induced motions. *Nonlinear Processes in Geophysics*, 19(6), 643–655.

Crosetto, M., Monserrat, O., Cuevas-González, M., Devanthéry, N., Crippa, B., 2016. Persistent scatterer interferometry: A review. *ISPRS Journal of Photogrammetry and Remote Sensing*, 115, 78–89.

De Martino, P., Dolce, M., Brandi, G., Scarpato, G., Tammaro, U., 2021. The ground deformation history of the Neapolitan volcanic area (Campi Flegrei caldera, Somma–Vesuvius Volcano, and Ischia island) from 20 years of continuous GPS observations (2000–2019). *Remote Sensing*, 13(14), 2725.

Delen, A., Balik Sanli, F., 2024. A statistical approach for the integration of multi-temporal InSAR and GNSS-PPP ground deformation measurements. *Sensors*, 24(1), 43.

Dickey, D. A., Fuller, W. A., 1979. Distribution of the estimators for autoregressive time series with a unit root. *Journal of the American Statistical Association*, 74(366a), 427–431.

European Environment Agency, 2024. European Ground Motion Service: Calibrated 2019–2023 (vector), Europe, yearly, Oct. 2024. Accessed: 2025-10-23.

Ferretti, A., Prati, C., Rocca, F., 2002. Permanent scatterers in SAR interferometry. *IEEE Transactions on Geoscience and Remote Sensing*, 39(1), 8–20.

Ghaderpour, E., Antonielli, B., Bozzano, F., Mugnozza, G. S., Mazzanti, P., 2024a. A fast and robust method for detecting trend turning points in InSAR displacement time series. *Computers & Geosciences*, 185, 105546.

Ghaderpour, E., Masciulli, C., Zocchi, M., Bozzano, F., Scarascia Mugnozza, G., Mazzanti, P., 2024b. Estimating reactivation times and velocities of slow-moving landslides via PS-InSAR and their relationship with precipitation in central Italy. *Remote Sensing*, 16(16), 3055.

Ghaderpour, E., Mazzanti, P., Bozzano, F., Mugnozza, G. S., 2024c. Ground deformation monitoring via PS-InSAR time series: An industrial zone in Sacco River Valley, central Italy. *Remote Sensing Applications: Society and Environment*, 34, 101191.

Giudicepietro, F., Casu, F., Bonano, M., De Luca, C., De Martino, P., Di Traglia, F., Di Vito, M. A., Macedonio, G., Manunta, M., Monterroso, F. et al., 2024a. First evidence of a geodetic anomaly in the Campi Flegrei caldera (Italy) ground deformation pattern revealed by DInSAR and GNSS measurements during the 2021–2023 escalating unrest phase. *International Journal of Applied Earth Observation and Geoinformation*, 132, 104060.

Giudicepietro, F., Casu, F., Bonano, M., De Luca, C., De Martino, P., Di Traglia, F., Di Vito, M. A., Macedonio, G., Manunta, M., Monterroso, F., Striano, P., Lanari, R., 2024b. Geodetic anomaly detection and analysis in the Campi Flegrei caldera (Italy) deformation pattern of the 2021–2023 escalating unrest phase. Dataset.

Hanssen, R. F., 2001. *Radar interferometry: Data interpretation and error analysis*. Kluwer Academic Publishers.

Hu, F., van Leijen, F. J., Chang, L., Wu, J., Hanssen, R. F., 2021. Combined detection of surface changes and deformation anomalies using amplitude-augmented recursive InSAR time series. *IEEE Transactions on Geoscience and Remote Sensing*, 60, 1–16.

Hussain, E., Novellino, A., Jordan, C., Bateson, L., 2021. Offline-online change detection for Sentinel-1 InSAR time series. *Remote Sensing*, 13(9), 1656.

Kingma, D. P., Ba, J., 2014. Adam: A method for stochastic optimization. *arXiv preprint arXiv:1412.6980*. https://arxiv.org/abs/1412.6980.

Kingma, D. P., Welling, M., 2013. Auto-encoding variational Bayes. *arXiv preprint arXiv:1312.6114*. https://arxiv.org/abs/1312.6114.

Lattari, F., Rucci, A., Matteucci, M., 2022. A deep learning approach for change points detection in InSAR time series. *IEEE Transactions on Geoscience and Remote Sensing*, 60, 1–16.

Matano, F., Casaburi, A., De Natale, G., 2025. An MT-InSAR-based procedure for detecting and interpreting vertical ground deformation anomalies during phases of unrest at Campi Flegrei caldera, Italy. *Applied Sciences*, 15(6), 3344.

Notti, D., Calò, F., Cigna, F., Manunta, M., Herrera, G., Berti, M., Meisina, C., Tapete, D., Zucca, F., 2015. A user-oriented methodology for DInSAR time series analysis and interpretation: Landslides and subsidence case studies. *Pure and Applied Geophysics*, 172(11), 3081–3105.

Omidalizarandi, M., Mohammadivojdan, B., Alkhatib, H., Paffenholz, J.-A., Neumann, I., 2023. On the quality checking of persistent scatterer interferometry data by spatial-temporal modelling. *Journal of Applied Geodesy*, 17(2), 119–131.

Osmanoğlu, B., Sunar, F., Wdowinski, S., Cabral-Cano, E., 2016. Time series analysis of InSAR data: Methods and trends. *ISPRS Journal of Photogrammetry and Remote Sensing*, 115, 90–102.

Polcari, M., Borgstrom, S., Del Gaudio, C., De Martino, P., Ricco, C., Siniscalchi, V., Trasatti, E., 2022. Thirty years of volcano geodesy from space at Campi Flegrei caldera (Italy). *Scientific Data*, 9(1), 728.

Raspini, F., Bianchini, S., Ciampalini, A., Del Soldato, M., Solari, L., Novali, F., Del Conte, S., Rucci, A., Ferretti, A., Casagli, N., 2018. Continuous, semi-automatic monitoring of ground deformation using Sentinel-1 satellites. *Scientific Reports*, 8(1), 7253.

Rodgers, J. L., Nicewander, W. A., 1988. Thirteen ways to look at the correlation coefficient. *The American Statistician*, 42(1), 59–66.

Shahryarinia, K., Omidalizarandi, M., Heidarianbaei, M. et al., 2025. Detecting change points in time series of InSAR persistent scatterers using deep learning models. *Applied Geomatics*, 17, 357–366.

Silverman, B. W., 1985. Some aspects of the spline smoothing approach to non-parametric regression curve fitting. *Journal of the Royal Statistical Society: Series B (Methodological)*, 47(1), 1–21.

Sinnott, R. W., 1984. Virtues of the Haversine. *Sky and Telescope*, 68(2), 158.

Srivastava, N., Hinton, G., Krizhevsky, A., Sutskever, I., Salakhutdinov, R., 2014. Dropout: A simple way to prevent neural networks from overfitting. *Journal of Machine Learning Research*, 15(1), 1929–1958.

Tondaś, D., Ilieva, M., van Leijen, F., van der Marel, H., Rohm, W., 2023. Kalman filter-based integration of GNSS and InSAR observations for local nonlinear strong deformations. *Journal of Geodesy*, 97(12), 109.

Virtanen, P., Gommers, R., Oliphant, T. E., Haberland, M., Reddy, T., Cournapeau, D., Burovski, E., Peterson, P., Weckesser, W., Bright, J. et al., 2020. SciPy 1.0: Fundamental algorithms for scientific computing in Python. *Nature Methods*, 17(3), 261–272.

Zhao, K., Wulder, M. A., Hu, T., Bright, R., Wu, Q., Qin, H., Li, Y., Toman, E., Mallick, B., Zhang, X. et al., 2019. Detecting change-point, trend, and seasonality in satellite time series data to track abrupt changes and nonlinear dynamics: A Bayesian ensemble algorithm. *Remote Sensing of Environment*, 232, 111181.